Publishing Excellence
Inspiring Progress
ARISTON PUBLICATIONS

Energy & Environment Advances

ISSN: xxxx-xxxx https://aristonpubs.com/energy-environment-advances https://doi.org/10.69626/eea.2024.0059

RESEARCH ARTICLE

Exploring the $BiVO_4/WO_3$ Hybrid System for Enhanced Photocatalytic Degradation and Hydrogen Evolution Reaction (HER)

Mansi Rana [1], Shivani Dangwal [1], Saurabh Rawat [1], Charu Dwivedi [2], Himani Sharma [1,*]

ABSTRACT: Dual functional heterostructure of Bismuth vanadate and Tungsten trioxide ($BiVO_4/WO_3$) was developed and its use in the generation of hydrogen and the degradation of dyes was shown. $BiVO_4$ was synthesized by the sol gel method, and its heterostructure with WO_3 was created by the solvothermal method. To study the morphological, structural, and optical characteristics of $BiVO_4$ and $BiVO_4/WO_3$, X-Ray diffraction (XRD), Field emission scanning electron microscope (FESEM), UV-visible spectroscopy (UV Vis), Raman spectroscopy and X-Ray photoelectron spectroscopy (XPS) was performed. Using Electrochemical Impedance Spectroscopy (EIS) and Linear Sweep Voltammetry (LSV), the electrochemical characteristics were ascertained. When exposed to visible light, $BiVO_4$ alone demonstrated a 73.4% degradation efficiency for methylene blue; however, the hybrid system yielded an 87.2% degradation efficiency. In the presence of 1M KOH solution an increase in current density and a lower value of onset potential (0.388 V vs RHE) was observed for the $BiVO_4/WO_3$. Similarly, EIS indicated a decrease in charge transfer resistance (83.92KΩ) in the case of hybrid. Better performance from the hybrid system in HER further presented its capacity to both clean up the environment and produce energy from renewable sources.

Keywords: $BiVO_4/WO_3$, Photocatalysis, Methylene blue, Electrochemical impedance spectroscopy (EIS).

Received: 27 February 2024; Revised: 21 March 2024; Accepted: 17 April 2024; Published Online: 08 May 2024

1. INTRODUCTION

In recent decades, there has been a growing interest in the field of photocatalysis, which is a fascinating process that involves the use of light to accelerate the rate of a chemical reaction. No doubt around the buzz, as the potential lies in its application towards building a safer and healthier environment for future generation. In this direction towards a sustainable and carbon zero world, we must develop reliable and clean renewable energy sources. This leads us to one of the current topic in this area of research, solar water splitting using semiconductor photocatalysts. This process allows the storing of solar energy by converting it into a different form. The ideal way of storing sunlight energy is in the form of hydrogen [1]. Solar water splitting has spurred extensive research, leading to the development of various potential catalysts [1, 2]. Thermodynamically, the amount of energy required for splitting water is about 1.23 eV, but considering the over-potential losses, the actual energy requirement ranges from 1.6 eV to 2eV [3].

Initially, photocatalytic studies were focused on binary metal oxides [4] made from abundant elements like TiO_2 [5], ZrO_2, α-Fe_2O_3, ZnO, and WO_3 [6], mainly because they're affordable and chemically durable. But there is a fundamental drawback to these binary metal oxides: their valence bands, which are usually made up of O 2p orbitals, limit the absorption of visible light and have an impact on the conduction band [4]. Recently, researchers have been exploring on elements like cerium, zinc, and bismuth vanadate which are ternary metal oxides, as a new photocatalysts for degradation of dyes and hydrogen production [7]. Among the semiconductor materials investigated for photocatalysis, bismuth vanadate ($BiVO_4$) stands out as a promising candidate as it shows excellent visible light absorption , appropriate bandgap, and exhibit

[1] Functional Nanomaterial Research Laboratory Department of Physics, Doon University, Dehradun-248001, India.
[2] Department of Chemistry, Doon University, Dehradun-248001, India.

* Author to whom correspondence should be addressed: hsharma.ph@doonuniversity.ac.in (Himani Sharma)

high stability [8]. Being a non-toxic yellow pigment that has been regarded as an extremely intriguing substitute, $BiVO_4$ has been widely used in pigment applications in previous years[9, 10]. The remarkable ferro-elasticity, gas-sensitive, coloristic qualities and ionic conductivity make bismuth vanadate very promising and have recently attracted the interest of researchers for possible applications like photocatalytic degradation and hydrogen evolution reactions. In addition, its narrow band gap of approximately 2.4 to 2.5 eV makes it an excellent photocatalyst for hydrogen generation and the decomposition of organic pollutants [11, 12]. Clinobisvanite, Pucherite and Dreyerite are the three polymorphs of $BiVO_4$, according to the literature. Clinobisvanite has monoclinic scheelite (m–s) structure, dreyerite shows tetragonal zircon (t–z) structure, and Pucherite is a naturally occurring polymorph of $BiVO_4$ with orthorhombic structure [13, 14]. Among the three phases, the monoclinic scheelite form exhibits greater coloristic qualities and significantly stronger photocatalytic ability when exposed to visible light [15, 16]. There are several ways to prepare the monoclinic scheelite phase of $BiVO_4$, like sol-gel method, hydrothermal treatment, coprecipitation method, or template method [17, 18]. Studies revealed that the $BiVO_4$ photocatalyst's low electron hole separation and tiny surface area made it unsuitable for photocatalysis [19]. In order to deal with this issue many approaches have been put forth, such as the creation of heterojunction structures [20], doping with metals or nonmetals [21], and the use of co-catalysts [22].

In this work, we aim to reduce recombination and enhance electron transport by utilizing tungsten trioxide (WO_3) to form a heterojunction. This will assist to address both of the issues that were present in $BiVO_4$. With a bandgap value between 2.7 and 2.9 eV, WO_3 is an indirect bandgap semiconductor. In terms of photo corrosion, it is extremely stable. Combining $BiVO_4/WO_3$ semiconductors can increase the system's absorption capacity. Apart from absorption, the heterojunction system has the potential to enhance the system's charge separation. Additionally, through facilitating electron separation between $BiVO_4$ and WO_3, the type 2 heterostructure that was developed substantially minimized charge recombination [23]. Moreover, the hybrid's oxygen vacancy enhances its charge separation which is necessary for the hydrogen evolution as well as the degradation of dyes.

In this research, we synthesized pure $BiVO_4$ using the sol-gel method, which is a versatile and cost-effective technique that allows for precise control over the material's composition and shape. And then created its heterostructure with WO_3 using the solvothermal method, which is known for producing highly crystalline materials with well-defined nanostructures. For the detailed information on the crystallinity, morphology, optical properties and charge transfer characteristics of the $BiVO_4$ and $BiVO_4/WO_3$ samples, various characterization techniques, including X-ray diffraction (XRD), Field emission scanning electron microscopy (FESEM), Micro Raman spectroscopy, UV-Vis spectroscopy, X ray photoelectron spectroscopy (XPS), linear sweep voltammetry (LSV), and electrochemical impedance spectroscopy (EIS) were used. We explored the combined effects of $BiVO_4$ and WO_3 in two important photocatalytic applications: breaking down methylene blue, a common organic dye used as a model pollutant, and the hydrogen evolution reaction (HER), which is a critical step in solar water splitting for sustainable hydrogen production. Numerous companies frequently utilize methylene blue dye, which raises serious environmental problems when it is found in water bodies. Real-world environmental uses of the $BiVO_4$-WO_3 heterostructure may be demonstrated if this dye could be efficiently broken down under visible light.

Our research showed that, although the pure $BiVO_4$ was degrading at a respectable pace, the hybrid was achieving remarkably higher rates of degradation. Along with pollutant degradation we also observed that in the case of $BiVO_4/WO_3$, HER activity was increased. To summarize, this research delves into the creation of a $BiVO_4/WO_3$ heterostructure and its use in the hydrogen evolution and photocatalytic degradation of methylene blue. This work enhances the development of effective photocatalysts for energy and environmental applications by overcoming the constraints of $BiVO_4$ through heterostructure creation. The results highlight the versatility and efficacy of the $BiVO_4/WO_3$ system as a photocatalyst, paving the way for further advancements in this area.

2. EXPERIMENTAL DETAILS

2.1. Synthesis of bismuth vanadate ($BiVO_4$)

The synthesis of bismuth vanadate ($BiVO_4$) powder using sol-gel method is shown in Figure 1. Initially bismuth nitrate pentahydrate ($Bi(NO_3)_3{\cdot}5H_2O$) and ammonium vanadate (NH_4VO_3) were utilized in the molar ratio of 1:1. In Solution 1, 0.7276 g of $Bi(NO_3)_3{\cdot}5H_2O$ in 50 ml of 4M nitric acid (HNO_3) was dissolved. On the other hand, 0.175 g of NH_4VO_3 was dissolved in 50 ml of 4M ammonium hydroxide (NH_4OH) for Solution 2. The two solutions, each of which consisted of Bi and V elements, were then mixed and stirred for 30 minutes, which finally led to the appearance of the yellow colour. And after that, ethanol (C_2H_5OH) of 100 ml was poured into the mixture, which was kept at 70°C while it was kept stirring for 1 hour. After that, 50 ml of DI and 5 ml of 1M acetic acid (CH_3COOH) were added to the yellow sol, which then turned into a yellow gel. It was dried in an oven for 48 hours at 100°C and then calcined in a muffle furnace at 500°C for 2 hours, the $BiVO_4$ obtained is thus marked as BVO.

2.2 Synthesis of tungsten trioxide (WO_3)

For the preparation of WO_3 powder, two solutions were initially prepared. For Solution A, 5 ml of 65% nitric acid (HNO_3) was added dropwise to 25 ml of DI, and for full dissolution the mixture was continuously stirred for 10

minutes. Parallel to this, for solution B 0.45g of sodium tungstate ($Na_2WO_4 \cdot 2H_2O$) was dissolved in 10 ml of DI, under continuous stirring until a transparent solution was achieved. After that, Solution B was gradually added to Solution A while stirring continually. This caused a white precipitate to gradually turn light yellow, signifying the development of precursors for tungsten trioxide. To make sure of consistency and a full reaction, the mixture was agitated for a further forty-five minutes. This homogenous mixture was processed hydrothermally for 24 hours at 180°C in a stainless-steel autoclave lined with Teflon. Centrifugation was then used to gather the yellow precipitate that resulted. The precipitate was then washed with ethanol and DI to remove any residual impurities or unreacted precursors. Finally, the cleaned product was dried for 6 hours at 60°C to obtain the final WO_3 powder (Figure 2). The synthesized WO_3 was named as WO.

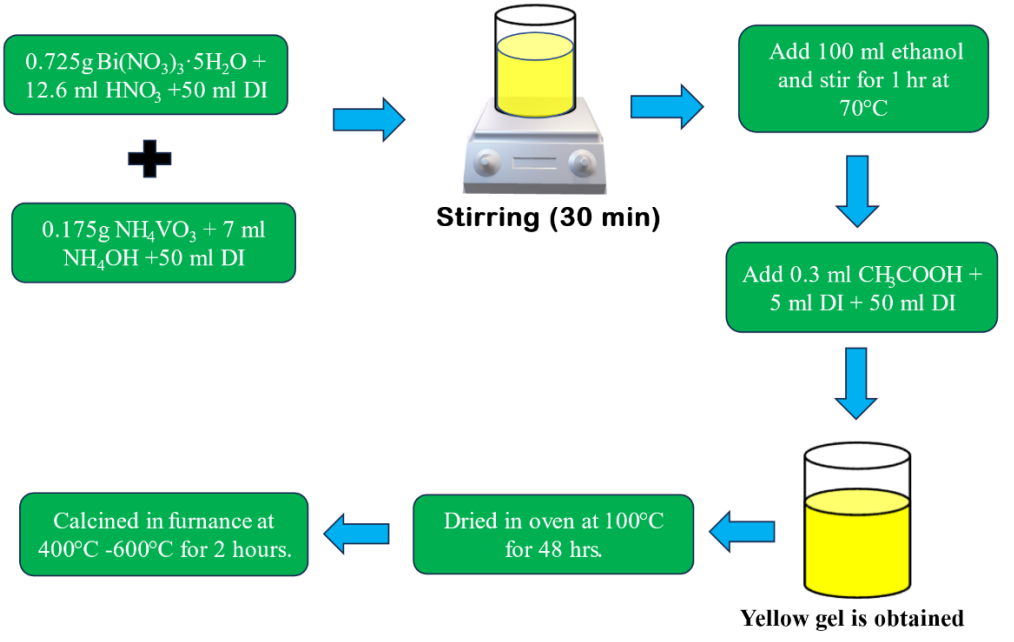

Fig. 1. Schematic diagram of synthesis of BVO powder using sol gel method.

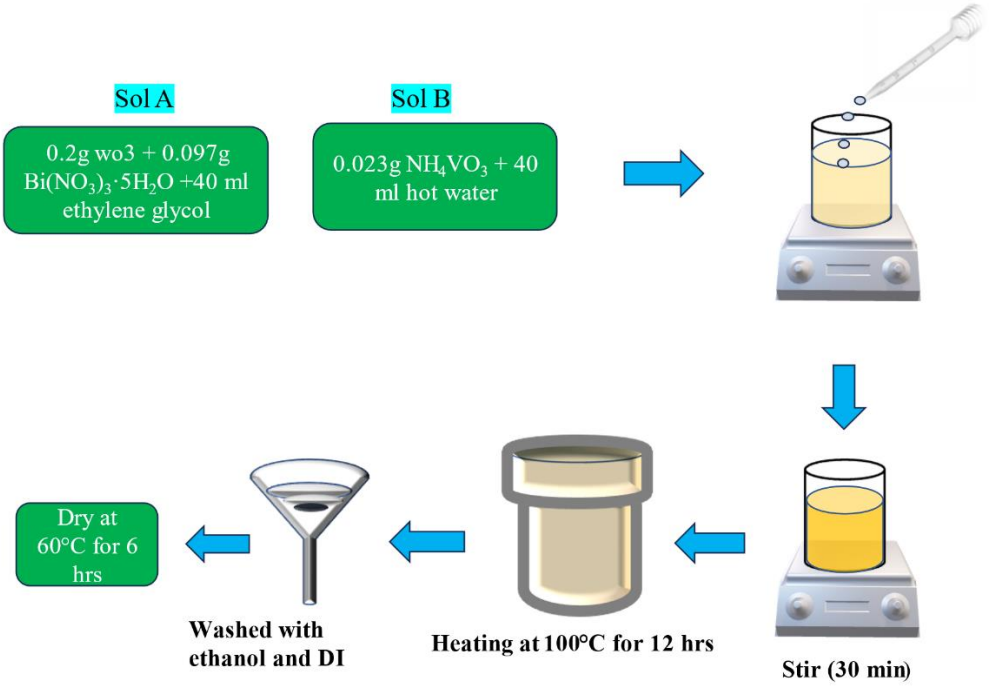

Fig. 2. Schematic diagram of synthesis of WO by hydrothermal method.

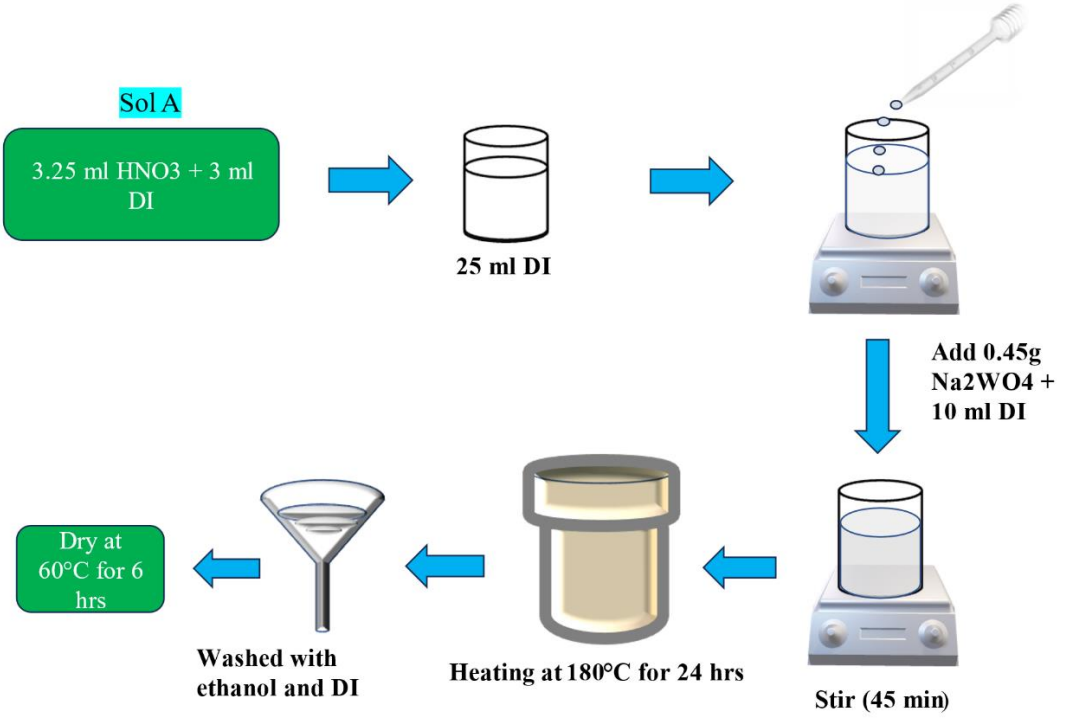

Fig. 3. Schematic diagram of synthesis of BVO/WO by solvothermal method.

2.3. Synthesis of $BiVO_4/WO_3$

For solution A, 40mL of ethylene glycol was used to dissolve 0.2g of WO_3 and 0.2mmol of $Bi(NO_3)_3$, while 40mL of hot water was used to dissolve a stoichiometric quantity of NH_4VO_3 in relation to $Bi(NO_3)_3$ for the preparation of sol B. To guarantee the solutes dissolved fully and produced a transparent, homogenous solution, two solutions were vigorously agitated. The $WO_3/Bi(NO_3)_3$ mixed solution was stirred while the NH_4VO_3 solution was gradually added. Following 30 minutes of magnetic stirring the aforementioned combined solution, the suspensions were placed in Teflon lined beaker and heated to 100 °C for a duration of 12 hours. After the resultants had cooled to room temperature, they were collected and thoroughly cleaned using ethanol and DI [24]. Lastly, the synthesized products were dried for six hours at 60°C to produce $BiVO_4/WO_3$ powders (Figure 3). The synthesized heterostructure was named as BVO/WO.

2.4. Photocatalytic activity test

To determine the photocatalytic activity, we measured the quantity of Methylene blue (MB) that degraded when exposed to visible light. For this we used a 300W Xenon lamp as the light source. A precise quantity of 50 mg BVO and 40 mL of concentrated MB (10 mg L^{-1}) were put in the solution. To achieve the adsorption equilibrium, the suspensions were magnetically agitated in the dark for 30 minutes after being ultrasonically sonicated for five minutes. Samples were taken at regular intervals of 15 minutes over the 90 minute degradation experiment. Prior to analysis, the collected samples underwent filtration and centrifugation for five minutes to eliminate any remaining catalyst particles. Then by plotting the absorbance vs wavelength graph, the extent of MB degradation was determined.

The Degradation efficiency (%) was calculated from the following expression:

$$\text{Degradation Efficiency (\%)} = \left(\frac{C_0 - C}{C_0}\right) * 100 \quad (1)$$

Where C_o is the initial concentration of MB and C is the concentration of MB at time t [25].

2.5. Electrochemical measurements

The measurements were conducted in 1M KOH solution as an electrolyte using BVO, BVO/WO drop casted on FTO as working electrode, Ag/AgCl and platinum wire were taken as reference and counter respectively. The electrochemical characteristics were assessed using EIS and LSV using an Admiral Squidstat electrochemical workstation. EIS was performed in the range of 100KHz–0.01Hz. LSV was taken at a scan rate of 10 mV s^{-1} in order to record the current density [26]. The obtained potential was converted into a RHE potential using the following equation:

$$E_{RHE} = E_{Ag/AgCl} + (0.0591 \times pH) + E_{Ag/AgCl^\circ} \quad (2)$$

Where E_{RHE} is reversible hydrogen electrode potential which is used as a reference scale to compare the potential of different electrode and $E_{Ag/AgCl} = 0.1976$ V.

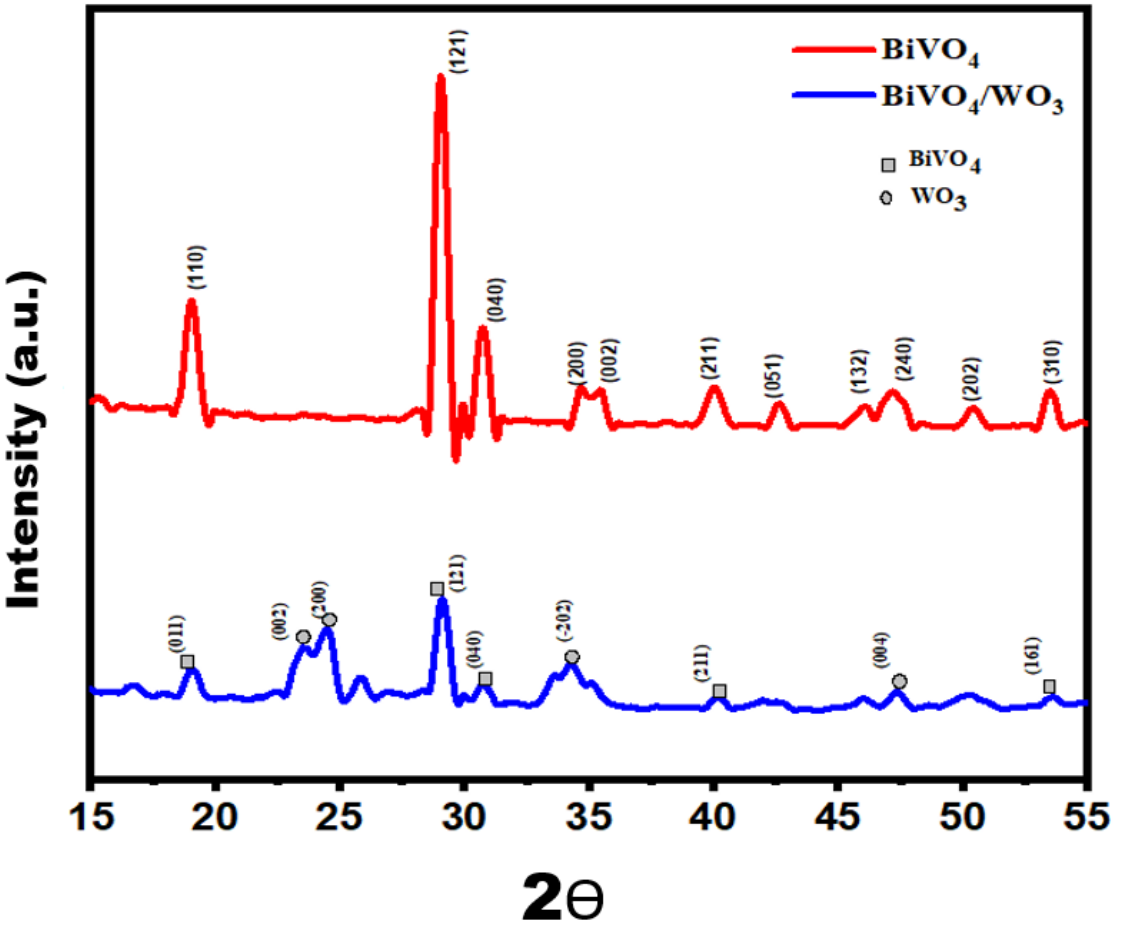

Fig. 4. X-Ray diffraction pattern of BVO and BVO/WO nanocomposites.

2.6. Material characterization

For the X-ray diffraction pattern, Panalytical X Pert Pro X-ray diffractometer was used. Carl Zeiss ultra plus field emission scanning electron microscope was utilized to determine the morphology of the synthesized nanostructures. To obtain the absorption spectrum, UV–vis spectroscopy was performed using Labman double beam spectrometer (LMSP-UV 1900S) from 400 nm 800 nm. Micro-Raman spectroscopy (Horiba-Jobin Yvon LABRAM spectrometer) was used to detect the vibrational modes. To examine the interfacial electronic interaction in the BVO/WO heterostructures an X-ray photoelectron spectroscopy was performed using VG ESCALAB 220I-XL.

3. RESULTS AND DISCUSSION

3.1 XRD analysis

The crystallinity of BVO and BVO/WO heterostructure were investigated using XRD. The XRD patterns, as illustrated in Figure 4, have different peaks for each substance. The pure BVO sample (red curve) shows distinctive diffraction peaks at 18.7°, 28.9°, 30.5°, 34.5°, and 47.2° corresponding to (110), (121), (040), (200), (240) planes. These peaks correlate to BVO's monoclinic scheelite structure (JCPDS 14-0688). The most intense peak at 28.9° corresponds to the (121) plane, showing a high crystallinity in the BVO sample [27-29]. The lattice parameters a, b, c was found to be 5.195 Å, 11.70 Å, 5.0920 Å respectively. The BVO/WO heterostructure (blue curve) has peaks from both BVO and WO. The composite diffraction peaks at 18.7°, 23.1°, 28.9°, 30.5°, 33.2°, and 34.5° correspond to the individual peaks of BVO and WO, respectively. This confirms the successful development of the heterostructure, which combines the crystalline features of both materials. The absence of additional peaks in the XRD pattern of BVO/WO heterostructure suggests that no new crystalline phases were formed throughout the synthesis [23]. Moreover, it has been demonstrated that for both BVO and WO their monoclinic structure shows excellent qualities. To determine the crystalline size of BVO and BVO/WO Debye Scherrer formula was used and is listed in Table 1.

$$\mathbf{D} = \frac{\mathbf{0.9\lambda}}{\boldsymbol{\beta cos\theta}} \quad (3)$$

where D is the size of crystallite, β is FWHM (radians),

λ is wavelength of x ray radiation (λ = 1.54), and θ = Bragg angle [30].

Table 1. Tabulation of BVO and WO crystalline sizes using Scherrer's formula.

Material	Crystalline size
BVO	21.378 nm
BVO/WO	13.865 nm

3.2. FESEM analysis

The morphology of pure BVO and BVO/WO were examined by FESEM. Figures 5 (a) and (b) show the FESEM images of pure BVO at different magnifications. The particles of BVO powder showed agglomerated morphology and was irregular due to the adsorbed addictive surfactants. The particle size was found to be 10-15 µm [27]. These particles appear to be polycrystalline as revealed by their rough and uneven surface. Figures 5 (c) and (d) shows the FESEM images of BVO/WO heterostructure. When WO is added to BVO, a noticeable change in the morphology appears. BVO/WO shows more definite, compact structure with bigger and uniformly spaced particle [31]. It seems that by adding WO, it improved the materials structural integrity which results in enhanced photocatalytic activity.

3.3. Raman spectral analysis

The Raman spectra of pure BVO and BVO/WO heterostructure confirmed the different vibrational modes of the BVO and WO phases which were represented by the varied peaks as seen in the Figure 6, which aid in verifying the synthesis and interaction of these materials. For the pure BVO sample, characteristic peaks are displayed at 113.3 cm^{-1}, 190.1 cm^{-1}, 336.5 cm^{-1}, and 808.7 cm^{-1} (red line). No more phase peaks were seen, and the peaks at 113.3 cm^{-1} and 190.1 cm^{-1} show the bending mode of Bi-O bonds in BVO, which validates the creation of the monoclinic phase. The symmetric bending mode of the V-O bonds in the VO_4 tetrahedrons is indicated by the peak at 336.5 cm^{-1}. Ultimately, the peak at 808.7 is attributed to the monoclinic scheelite BVO's symmetric stretching mode of V–O which is its hall mark peak with Ag symmetry. Additional peaks are seen at 182.5 cm^{-1}, 250.7 cm^{-1}, 314.7 cm^{-1}, 709.17 cm^{-1}, and 802.7 cm^{-1} in the BVO/WO heterostructure (blue line). We may ascribe the additional peak at 250.7 cm^{-1} to the W-O stretching modes of WO. In WO, the symmetric stretching mode of the W-O-W bonds is represented by the peak at 709.17 cm^{-1}. The development of the BVO/WO heterostructure and the interaction between BVO and WO are indicated by the little shift in peak positions and the appearance of new peaks [32, 33]. Thus, the combined Raman spectra validate the successful fabrication of BVO/WO heterostructures and offer information about the vibrational properties of composite material.

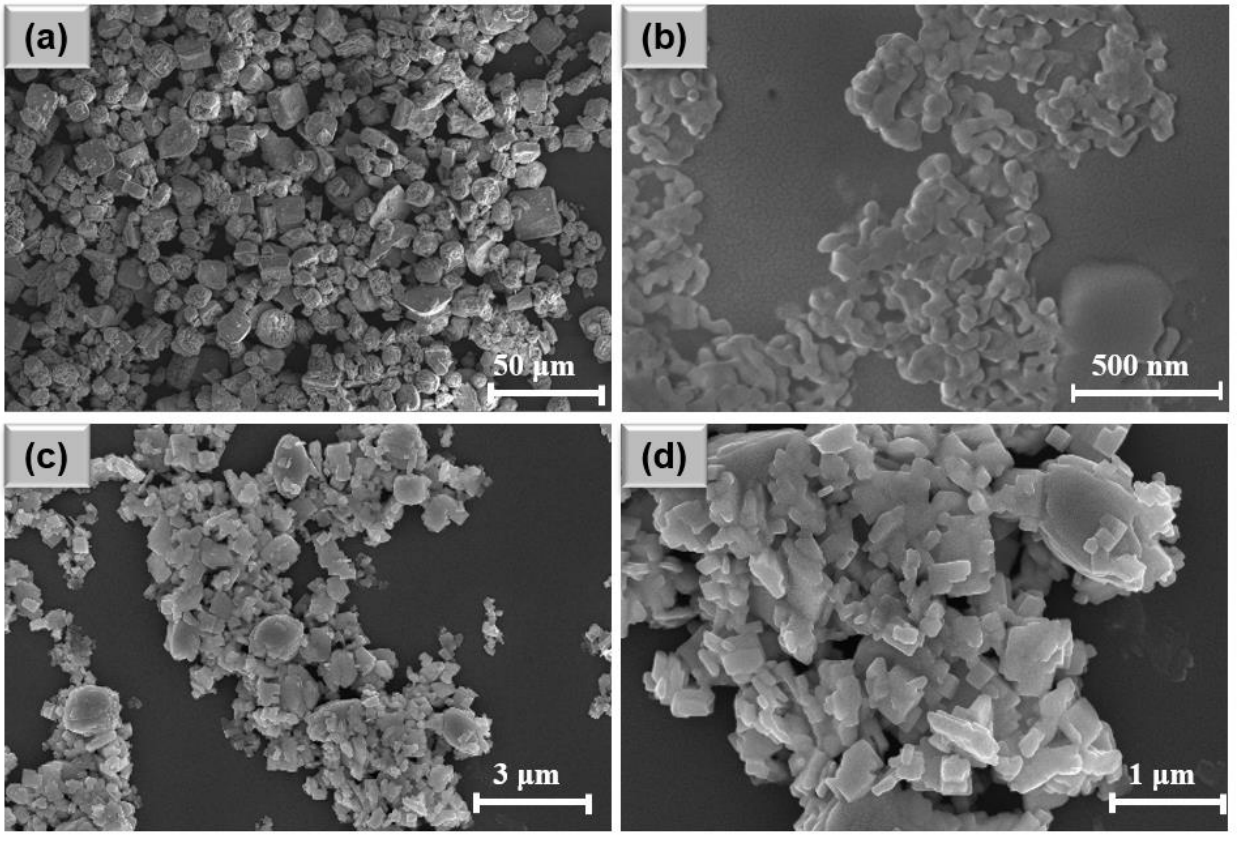

Fig. 5. FESEM images of (a, b) BVO, and BVO/WO nanocomposite.

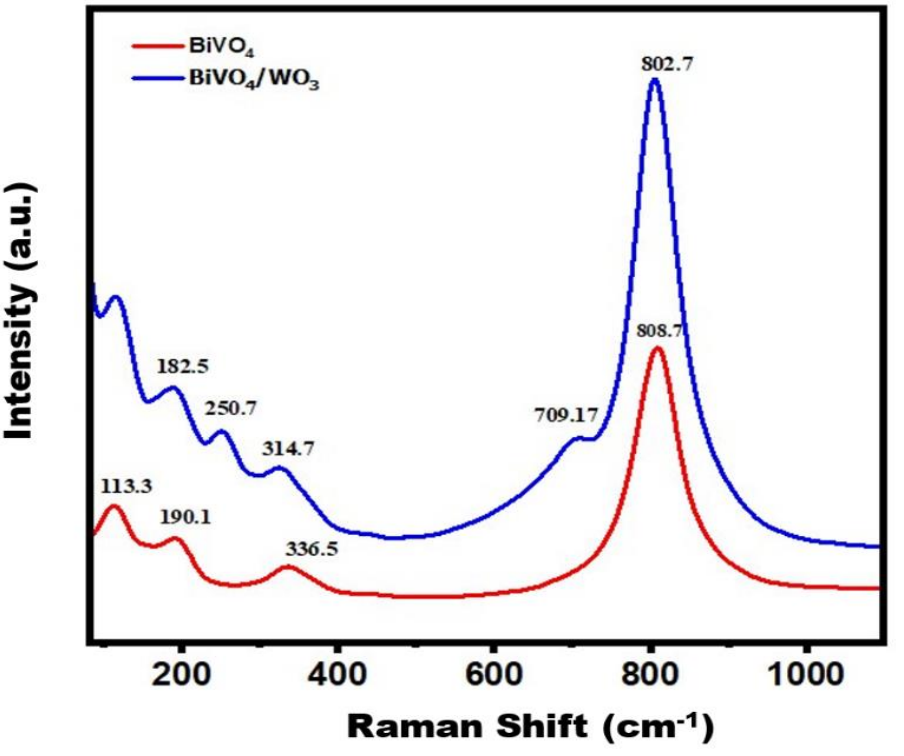

Fig. 6. Raman spectrum of BVO and BVO/WO indicating the vibrational stretching and bending modes.

3.4. UV Vis spectroscopy

Efficient light absorption in photocatalytic and electrocatalytic applications depends on the optical properties of BVO/WO. Figure 7 shows the Tauc's plot of BVO and BVO/WO heterojunction to determine its band gap. The absorption of bare BVO, with band gap 2.6eV, is seen at 490 nm. This makes it a direct bandgap semiconductor. In comparison to pure BVO, the BVO/WO hybrid's UV-Vis absorption spectra exhibit an absorption edge at a longer wavelength and showed that its band gap energy decreased. The hybrid's Tauc plot indicates that its band gap energy is roughly 2.0 eV. The incorporation of WO into the BVO matrix effectively narrows the band gap, which enhances the material's ability in absorbing visible light and improve its photocatalytic performance. The reduction in band gap energy for the hybrid is due to the synergistic effect between BVO and WO, as new energy levels are introduced within the band gap and enable electron transition with less energy [34]. Additionally, the strain brought on by lattice mismatch and effective charge transfer between components is what causes the band gap to decrease. The presence of WO not only narrows the band gap but also enhances the separation of electron-hole pairs which further leads to the improved photocatalytic efficiency of hybrid.

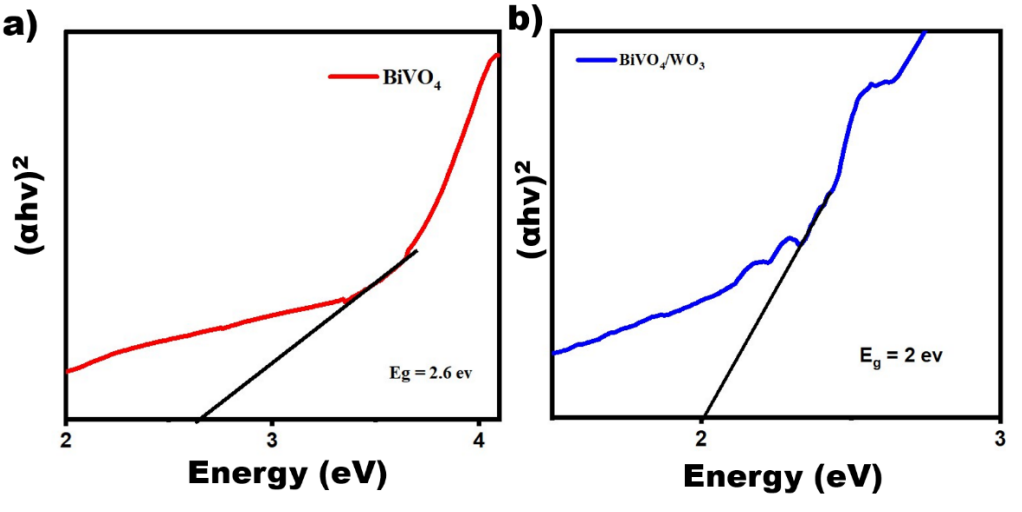

Fig. 7. Tauc's plot to determine the energy bandgap of BVO and BVO/WO.

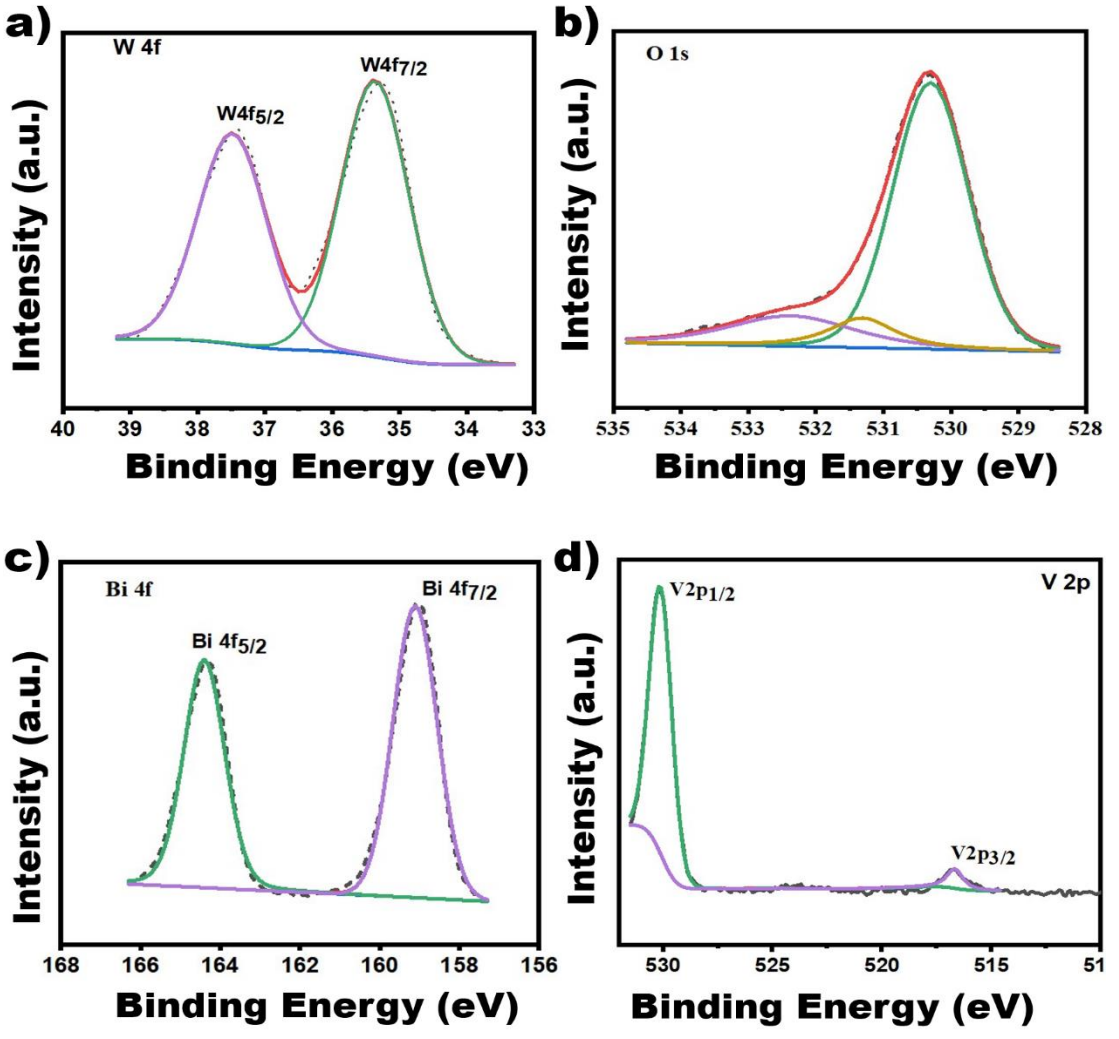

Fig. 8. XPS spectra of BVO/WO hybrid, (a) W 4f, (b) O 1s, (c) Bi 4f, and (d) V 2p. These peaks confirmed the presence of the elements in heterostructure.

3.5. XPS analysis

XPS was utilized to examine the electronic configurations of the BVO/WO in order to verify the presence of elements in the hybrid. In Figure 8(a–d), high resolution spectra for the elements (W, O, Bi, and V) are shown, respectively. As displayed in Figure 8(a), peaks for W 4f at 35.3 eV and 37.4 eV of the W^{6+} state was observed (corresponding to W $4f_{7/2}$ and W $4f_{5/2}$ respectively) [35]. In case of O 1s spectra in Figure 8(b) peak at 530.1 eV were observed suggesting the presence of oxygen species which correspond to the lattice oxygen in metal oxides (O Lattice). The peak at 531.4 eV correspond to surface defects (O vacancy) and that at 532.5 eV correspond to surface absorbed oxygen (O surface) as reported previously. Two typical peaks, corresponding to Bi $4f_{7/2}$ and Bi $4f_{5/2}$ of the Bi^{3+} state, can be seen in Figure 8(c) at 159.4 and 164.3 eV. In addition, V 2p spectra with two peaks at 516.9 and 529.7 eV are displayed in Figure 8(d). These peaks associated to V $2p_{3/2}$ and V $2p_{1/2}$ of the V^{5+} state, respectively [23].

3.6. Photocatalytic activity

By observing the breakdown of MB in an aqueous solution (10 ppm) under visible light irradiation, the photocatalytic activity of the BVO and BVO/WO samples was assessed. In Figure 9, it is seen that after 90 minutes of exposure to visible light, 73.45% of the MB dye was degraded when BVO was present, and 87.22% of the MB dye was degraded when BVO/WO was present. The outcomes demonstrated that compared to pure BVO, the BVO/WO heterostructure shows better photocatalytic performance as compared to pristine sample. On excitation under light, electron–hole pairs are produced in the nanocomposite. This low-power visible light is enough to excite the BVO photocatalyst because of its low band gap. The recombination process is one of the key elements of photocatalysis reactions. This is particularly true for semiconductors with fragile band gaps. The efficiency of the photocatalytic processes is reduced by the recombination process. Because WO is present in a BVO/WO nanocomposite, the prepared electron–hole pairs migrate to

WO and eventually reach the photocatalyst surface. As a result, this nanocomposite's photocatalytic reaction has a reduced recombination process. In addition to WO's strong charge conductivity, more charges migrate to the photocatalyst surface. The strong photocatalytic activity of the produced BVO/WO hybrid is due to the synergistic impact of WO and BVO, good adjustment between the valence and conduction bands of WO and BVO, and optimal composition between these two components. Figure 10 depicts the schematic diagram for the MB degradation over BVO/WO.

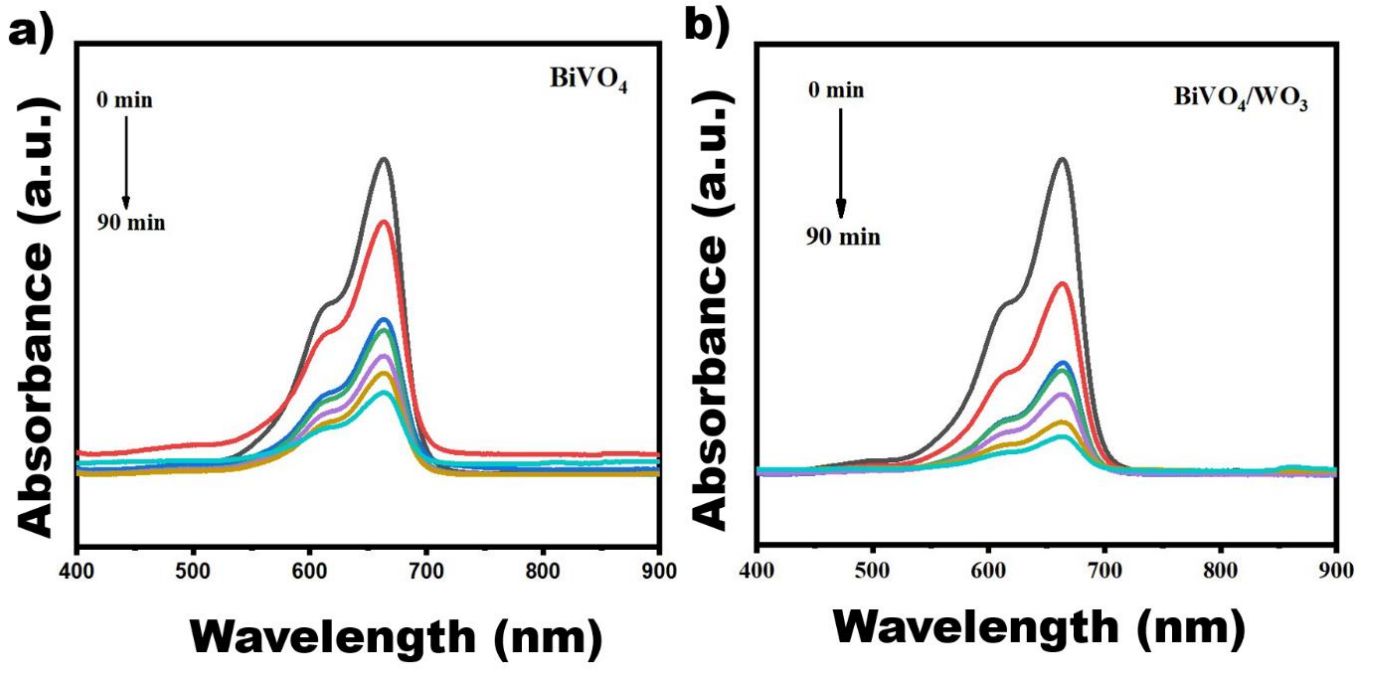

Fig. 9. UV VIS spectra indicating the degradation of MB a) in the presence of BVO b) in the presence of BVO/WO for 90 min.

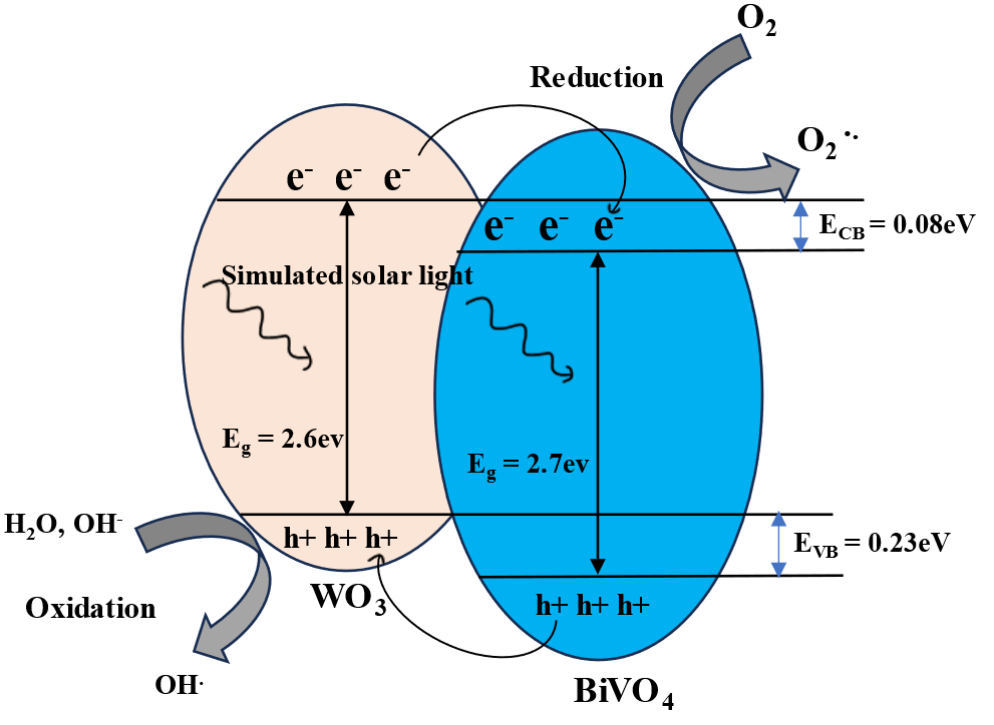

Fig. 10. Schematic diagram of MB degradation over BVO/WO.

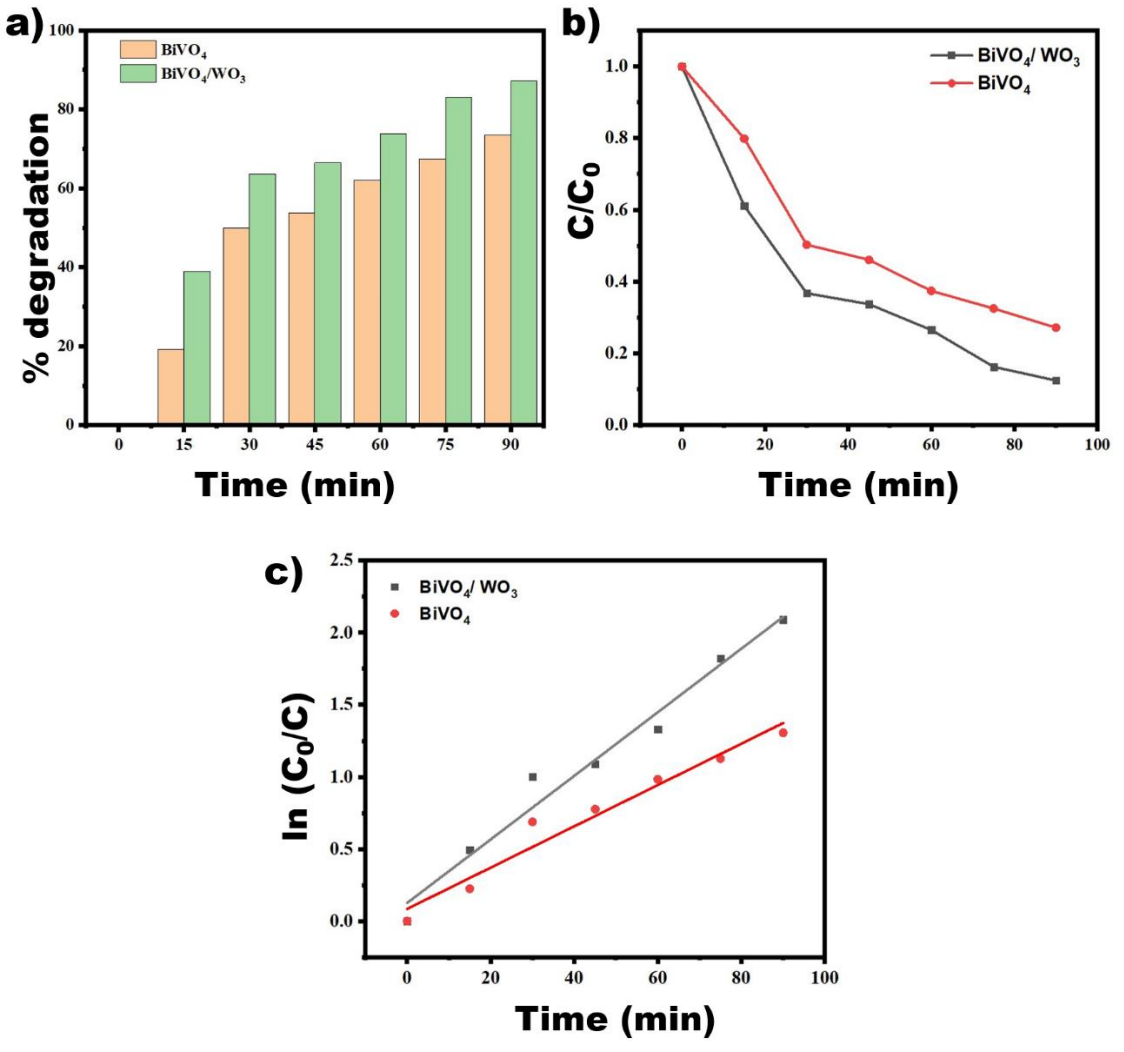

Fig. 11. (a) Percentage degradation graph of pure BVO and BVO/WO, (b) plots of C/C_0 vs time, and (c) kinetics of photodegradation of MB.

The better photocatalytic activity of BVO/WO nanoparticles is highly correlated with the number of surface hydroxyl groups. As the amount of surface hydroxyl groups increases, its photocatalytic activity is enhanced [36]. Figure 11 (a) displays the percentage degradation graph of BVO, BVO/WO, and Figure 11 (b) depicts the change in MB concentration. Langmuir Hinshelwood kinetic formula was used to illustrate the Kinetics of the photodegradation of MB over BVO and BVO/WO photocatalysts, according to the equation:

$$\ln\left(\frac{CO}{CT}\right) = kt \quad (4)$$

Where k is the observed rate constant [37]. The kinetic plot of MB's degradation data is displayed in Figure 11 c and the correlation coefficient (R^2) was calculated and it showed that photodegradation of MB follows pseudo first order kinetics (Table 2).

The kinetic results further show that, for the dye degradation, the BVO/WO nanoparticle exhibits a larger rate constant than BVO. Hence, we can conclude heterostructure acts as a good photocatalyst as compared to BVO.

Table 2. Kinetic value for the photocatalytic degradation of MB in the presence of BVO and BVO/WO.

Photocatalyst	Rate constant (K)	% degradation	R^2
BVO	0.014	73.45	0.953
BVO/WO	0.022	87.22	0.974

3.7. Electrochemical measurements

The electrocatalytic activity of synthesized BVO and BVO/WO heterostructure was evaluated by measuring the linear sweep voltammetry. Figure 12 (a) shows the LSV curve of BVO and BVO/WO in the presence of 1M KOH electrolyte. For both catalysts, an increase in current density

was seen with a voltage rise. BVO/WO heterostructure exhibits lower onset potential of 0.388V vs RHE as compared to pure BVO which is 0.523 V vs RHE as shown in the graph. As evidenced by this reduced onset potential, BVO/WO commences the HER process more effectively and uses less energy to start the reaction then BVO. The generated current density of BVO/WO was found to be higher than BVO due to the reduced electron hole recombination and improved charge separation which enhances the availability of charge carriers. Mechanism of HER in basic electrolyte, can be described by 2 methods Volmer - Heyrovsky and Volmer-Tafel method. In the Volmer step one proton (H^+) from the electrolyte adsorbs onto the catalyst surface and then combines with an electron (e^-) and forms an adsorbed hydrogen atom. In Heyrovsky Step, another proton (H^+) from the solution combines with the adsorbed hydrogen atom and an electron (e^-) and produces hydrogen gas (H_2). Similarly, in Tafel step two adsorbed hydrogen atoms combines and forms hydrogen gas (H_2), which then desorbs from the catalyst surface [38].

$$(H^+ + e^- \rightarrow H_{ads}) \quad (5)$$

$$(H_{ads} + H^+ + e^- \rightarrow H_2) \quad (6)$$

$$(2H_{ads} \rightarrow H_2) \quad (7)$$

In addition to onset potential, the Tafel slope is a crucial criterion for assessing catalysts' HER performance. The Tafel value could be used to study the electrocatalytic activities of catalysts and explain the HER mechanism. It also provides an explanation for the HER process's rate-determining step (RDS) and microkinetic analysis. When the Tafel slope is less, lower overpotential is needed to produce the same current density increment, resulting in faster electron-transfer kinetics during the reduction-oxidation process. Small Tafel slope and high exchange current density are characteristics of a high-performance electrocatalyst[39, 40]. Figure 12 (b) displays the Tafel plots that were obtained from the LSV curves. By fitting the linear component of the plots, Tafel slopes were determined. The Tafel plots reveal a slope of BVO 91.4 mV/dec and BVO/WO 62 mV/dec. In real-world scenarios, a smaller Tafel slope is advantageous as it can lead to a quicker increase in the HER rate as overpotentials grow [41]. Literature states that the Volmer, Heyrovsky, and Tafel reaction mechanisms are associated with Tafel slopes of about 120 mV/decade, 40 mV/decade, and 30 mV/decade, respectively [42-45]. As a result, the reaction is of the Volmer-Heyrovsky type in our case since the Tafel slope of the BVO and BVO/WO heterostructure lies between the Volmer Heyrovsky range.

Furthermore, EIS was performed to determine the charge transfer resistance and electrochemical properties for the HER activity [46]. Figure 13 depicts the EIS spectra (Nyquist plot) of BVO and BVO/WO. To obtain the charge transfer resistance the circuit was fitted and then the values were found to be 3942 KΩ for BVO and 83.92KΩ for BVO/WO. The heterostructure proved to have the lowest charge transfer resistance (R_{ct}) based on the spectrum as compared to BVO or the H^+ reduction in the case of BVO as the electrode is more difficult [47] because of the better conductivity of WO. The fact that bare BVO has the greatest R_{ct}, its inadequate diffusion length and trap sites could be the cause of this. The band locations of WO and BVO in the case of heterojunction operate as a driving factor for the extraction of charge carriers. As a result, the BVO/WO R_{ct} decreases. Also, the synergistic effect between BVO and WO lowers the energy barrier of heterostructure for charge transfer. This leads to a reduced R_{ct} value and indicate towards more efficient charge transfer across the interface. Overall, these findings show that the BVO/WO heterostructure exhibits better electrocatalytic behaviour and performs better in terms of HER activity than the pure BVO material.

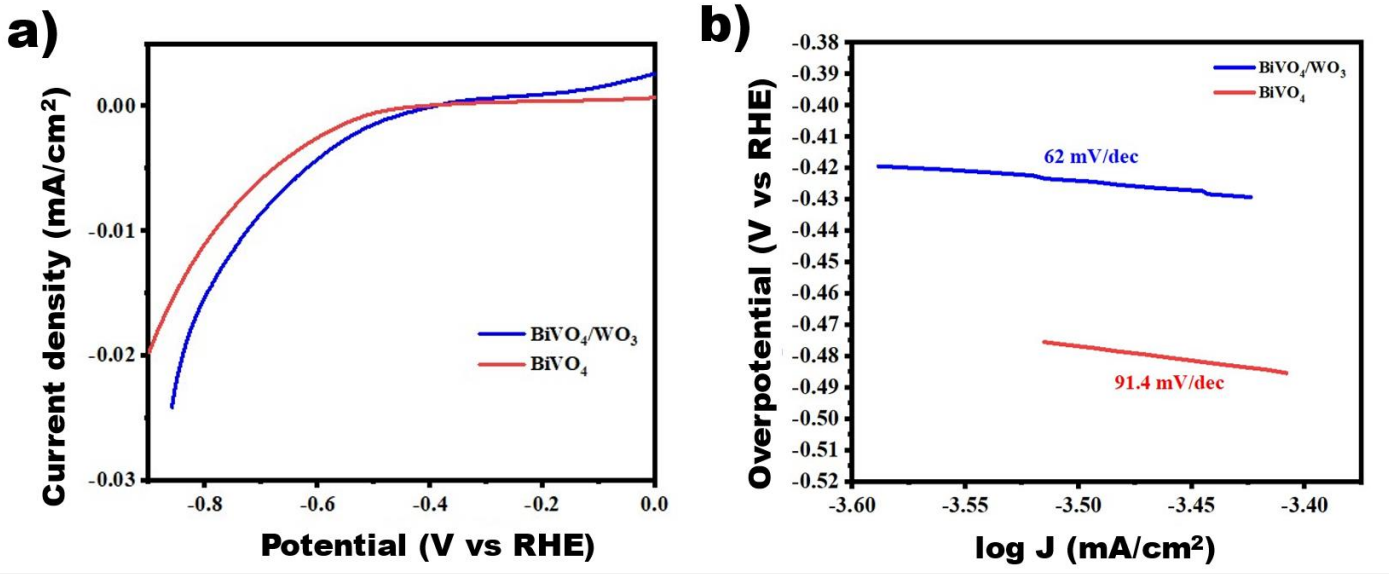

Fig 12. (a) Linear sweep voltammetry curve of BVO and BVO/WO showing the onset potential and current density, and (b) Tafel slope derived from LSV of BVO and BVO/WO hybrid.

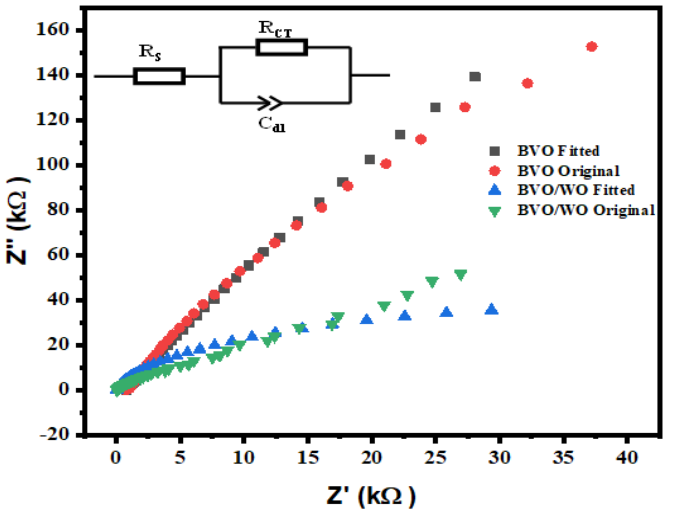

Fig 13. Electrochemical impedance spectroscopy with equivalent circuit model and Nyquist plots of experimental and fitted results for BVO and BVO/WO.

4. CONCLUSION

To summarize, a simple sol gel technique was employed to effectively create BVO nanoparticles, while a solvothermal approach was employed to create BVO/WO heterostructures. The synthesis of BVO and BVO/WO was confirmed by XRD, FESEM, XPS and RAMAN spectral data. The band gap of BVO, which is equal to 2.6 eV, fell to 2 eV in the case of the hybrid, according to UV-VIS spectroscopy, as new energy levels are introduced within the band gap and enable electron transition with less energy. Additionally, the strain brought on by lattice mismatch and effective charge transfer between components is what causes the band gap to decrease. In the photocatalytic degradation experiment, pure BVO decomposed the MB dye up to 73.45%, whereas BVO/WO allowed the dye to degrade up to 87.22%, demonstrating the superiority of BVO/WO as a photocatalyst. BVO/WO utilize the advantages of WO's enhanced electron transport and BVO's strong photocatalytic activity from their monoclinic structure. In the presence of a 1M KOH electrolyte, an increase in current density was observed. The enhanced current density of BVO/WO may be ascribed to the combined influence of the type 2 heterostructure, superior crystal structure, and oxygen vacancies. The onset potential for BVO was determined to be 0.522 V vs RHE, while for hybrid, it lowered to 0.388V vs RHE. With the use of the LSV curves, the Tafel slopes were computed to understand the electrode kinetics. BVO/WO showed a Tafel slope of 62 mV/dec which was less than BVO (91.4 mV/dec). The EIS analysis revealed that BVO/WO has low charge transfer resistance (83.92KΩ) than pure BVO (3942 KΩ). Overall, these results demonstrate that the BVO/WO heterostructure has superior electrocatalytic and photocatalytic activity.

DECLARATIONS

Ethical Approval

We affirm that this manuscript is an original work, has not been previously published, and is not currently under consideration for publication in any other journal or conference proceedings. All authors have reviewed and approved the manuscript, and the order of authorship has been mutually agreed upon.

Funding

Not applicable

Availability of data and material

All of the data obtained or analyzed during this study is included in the report that was submitted.

Conflicts of Interest

The authors declare that they have no financial or personal interests that could have influenced the research and findings presented in this paper. The authors alone are responsible for the content and writing of this article.

Authors' contributions

All authors contributed equally in the preparation of this manuscript.

ACKNOWLEDGEMENTS

The authors of this article express their sincere gratitude to Doon University Dehradun for its facilities. The Department of Science and Technology (DST), Government of India, is acknowledged by the authors for providing funding for research under the PURSE initiative (SR/PURSE/2023/199(G)). The authors acknowledge the Department of Science and Technology (DST), Government of India, for providing the Raman Spectroscopy facility (SR/FST/PSI225/2016) for the FST scheme.

REFERENCES

[1] Sitaaraman, S.R., Shanmugapriyan, M.I., Varunkumar, K., Grace, A.N. and Sellappan, R., **2021.** Synthesis of heterojunction tungsten oxide (WO_3) and Bismuth vanadate ($BiVO_4$) photoanodes by spin coating method for solar water splitting applications. *Materials Today: Proceedings*, *45*, pp.3920-3926.

[2] Lamm, B., Trzesniewski, B.J., Doscher, H., Smith, W.A. and Stefik, M., **2017**. Emerging postsynthetic improvements of $BiVO_4$ photoanodes for solar water splitting. *ACS Energy Letters*, *3*(1), pp.112-124.

[3] Su, J., Guo, L., Bao, N. and Grimes, C.A., **2011.** Nanostructured $WO_3/BiVO_4$ heterojunction films for efficient photoelectrochemical water splitting. *Nano Letters*, *11*(5), pp.1928-1933.

[4] Abraham, S.D., David, S.T., Bennie, R.B., Joel, C. and Kumar, D.S., 2**016.** Eco-friendly and green synthesis of $BiVO_4$ nanoparticle using microwave irradiation as photocatalayst for the degradation of Alizarin Red S. *Journal of Molecular Structure*, *1113*, pp.174-181.

[5] Cho, I.S., Choi, J., Zhang, K., Kim, S.J., Jeong, M.J., Cai, L., Park, T., Zheng, X. and Park, J.H., **2015.** Highly efficient solar water splitting from transferred TiO_2 nanotube arrays. *Nano Letters*, *15*(9), pp.5709-5715.

[6] Ronconi, F., Syrgiannis, Z., Bonasera, A., Prato, M., Argazzi, R., Caramori, S., Cristino, V. and Bignozzi, C.A., **2015.** Modification of nanocrystalline WO_3 with a dicationic perylene bisimide: applications to molecular level solar water splitting. *Journal of the American Chemical Society*, *137*(14), pp.4630-4633.

[7] Zhang, Z., Wang, W., Shang, M. and Yin, W., **2010.** Photocatalytic degradation of rhodamine B and phenol by solution combustion synthesized $BiVO_4$ photocatalyst. *Catalysis Communications*, *11*(11), pp.982-986.

[8] El-Hakam, S.A., ALShorifi, F.T., Salama, R.S., Gamal, S., El-Yazeed, W.A., Ibrahim, A.A. and Ahmed, A.I., **2022.** Application of nanostructured mesoporous silica/bismuth vanadate composite catalysts for the degradation of methylene blue and brilliant green. *Journal of Materials Research and Technology*, *18*, pp.1963-1976.

[9] Sun, W., Xie, M., Jing, L., Luan, Y. and Fu, H., 2011. Synthesis of large surface area nano-sized $BiVO_4$ by an EDTA-modified hydrothermal process and its enhanced visible photocatalytic activity. *Journal of Solid State Chemistry*, *184*(11), pp.3050-3054.

[10] Yao, M., Liu, M., Gan, L., Zhao, F., Fan, X., Zhu, D., Xu, Z., Hao, Z. and Chen, L., **2013**. Monoclinic mesoporous $BiVO_4$: Synthesis and visible-light-driven photocatalytic property. *Colloids and Surfaces A: Physicochemical and Engineering Aspects*, *433*, pp.132-138.

[11] Park, H.S., Kweon, K.E., Ye, H., Paek, E., Hwang, G.S. and Bard, A.J., **2011.** Factors in the metal doping of $BiVO_4$ for improved photoelectrocatalytic activity as studied by scanning electrochemical microscopy and first-principles density-functional calculation. *The Journal of Physical Chemistry C*, *115*(36), pp.17870-17879.

[12] Tahir, B., Tahir, M. and Amin, N.S., **2015.** Performance analysis of monolith photoreactor for CO_2 reduction with H_2. *Energy Conversion and Management*, *90*, pp.272-281.

[13] Bhattacharya, A.K., Mallick, K.K. and Hartridge, A., **1997.** Phase transition in $BiVO_4$. *Materials Letters*, *30*(1), pp.7-13.

[14] Park, Y., McDonald, K.J. and Choi, K.S., **2013.** Progress in bismuth vanadate photoanodes for use in solar water oxidation. *Chemical Society Reviews*, *42*(6), pp.2321-2337.

[15] Zhang, L., Chen, D. and Jiao, X., **2006.** Monoclinic structured $BiVO_4$ nanosheets: hydrothermal preparation, formation mechanism, and coloristic and photocatalytic properties. *The Journal of Physical Chemistry B*, *110*(6), pp.2668-2673.

[16] Hooda, A., Rawat, P. and Vaya, D., **2023.** Insight into the synthesis and photocatalytic applications of bismuth vanadate-based nanocomposites. *Current Nanoscience*, *19*(5), pp.697-714.

[17] Wu, Q., Chen, P., Zhao, L., Wu, J., Qi, X. and Yao, W., **2014.** Photocatalytic behavior of $BiVO_4$ immobilized on silica fiber via a combined alcohol-thermal and carbon nanofibers template route. *Catalysis Communications*, *49*, pp.29-33.

[18] Lin, X., Yu, L., Yan, L., Li, H., Yan, Y., Liu, C. and Zhai, H., **2014.** Visible light photocatalytic activity of $BiVO_4$ particles with different morphologies. *Solid state sciences*, *32*, pp.61-66.

[19] Ai, Z., Ho, W. and Lee, S., **2011.** Efficient visible light photocatalytic removal of NO with BiOBr-graphene nanocomposites. *The Journal of Physical Chemistry C*, *115*(51), pp.25330-25337.

[20] Wang, W., Huang, X., Wu, S., Zhou, Y., Wang, L., Shi, H., Liang, Y. and Zou, B., **2013.** Preparation of p–n junction $Cu_2O/BiVO_4$ heterogeneous nanostructures with enhanced visible-light photocatalytic activity. *Applied Catalysis B: Environmental*, *134*, pp.293-301.

[21] Zhao, Z., Dai, H., Deng, J., Liu, Y. and Au, C.T., **2013**. Enhanced visible-light photocatalytic activities of porous olive-shaped sulfur-doped $BiVO_4$-supported cobalt oxides. *Solid State Sciences*, *18*, pp.98-104.

[22] Tan, G., Zhang, L., Ren, H., Huang, J., Yang, W. and Xia, A., **2014.** Microwave hydrothermal synthesis of N-doped $BiVO_4$ nanoplates with exposed (040) facets and enhanced visible-light photocatalytic properties. *Ceramics International*, *40*(7), pp.9541-9547.

[23] Peerakiatkhajohn, P., Yun, J.H., Butburee, T., Lyu, M., Takoon, C. and Thaweesak, S., 2023. Dual functional $WO_3/BiVO_4$ heterostructures for efficient photoelectrochemical water splitting and glycerol degradation. *RSC Advances*, *13*(27), pp.18974-18982.

[24] Saraswathi, P., Ramarao, S.D., Kumar, R.A., Rajesh, C. and Rao, A.V., **2019.** Solvothermal synthesis of $BiVO_4/WO_3$ heterostructures and their applicability towards electrochemical water oxidation reactions. *The European Physical Journal Plus*, *134*(5), p.186.

[25] Farzadkia, M., Bazrafshan, E., Esrafili, A., Yang, J.K. and Shirzad-Siboni, M., **2015.** Photocatalytic degradation of Metronidazole with illuminated TiO_2 nanoparticles. *Journal of Environmental Health Science and Engineering*, *13*, pp.1-8.

[26] Park, E., Yoo, J. and Lee, K., **2024.** Enhanced photoelectrochemical hydrogen production via linked $BiVO_4$ nanoparticles on anodic WO_3 nanocoral structures. *Sustainable Energy & Fuels*, *8*(7), pp.1448-1456.

[27] Pookmanee, P., Paosorn, S. and Phanichphant, S., **2010.** Chemical Synthesis and characterization of bismuth vanadate powder. *Advanced Materials Research*, *93*, pp.153-156.

[28] Shen, Y., Huang, M., Huang, Y., Lin, J. and Wu, J., **2010.** The synthesis of bismuth vanadate powders and their photocatalytic properties under visible light irradiation. *Journal of Alloys and Compounds*, *496*(1-2), pp.287-292.

[29] Pookmanee, P., Paosorn, S. and Phanichphant, S., **2010.** Chemical Synthesis and characterization of bismuth vanadate powder. *Advanced Materials Research*, *93*, pp.153-156.

[30] Fatimah, S., Ragadhita, R., Al Husaeni, D.F. and Nandiyanto, A.B.D., **2022.** How to calculate crystallite size from x-ray diffraction (XRD) using Scherrer method. *ASEAN Journal of Science and Engineering*, *2*(1), pp.65-76.

[31] González-Borrero, P.P., Sato, F., Medina, A.N., Baesso, M.L., Bento, A.C., Baldissera, G., Persson, C., Niklasson, G.A., Granqvist, C.G. and Ferreira da Silva, A., **2010.** Optical band-gap determination of nanostructured WO_3 film. *Applied Physics Letters*, *96*(6).

[32] Yoon, H., Mali, M.G., Kim, M.W., Al-Deyab, S.S. and Yoon, S.S., **2016.** Electrostatic spray deposition of transparent tungsten oxide thin-film photoanodes for solar water splitting. *Catalysis Today*, *260*, pp.89-94.

[33] Rassoolkhani, A.M., Cheng, W., Lee, J., McKee, A., Koonce, J., Coffel, J., Ghanim, A.H., Aurand, G.A., Soo Kim, C., Ik Park, W. and Jung, H., 2019. Nanostructured bismuth vanadate/tungsten oxide photoanode for chlorine production with hydrogen generation at the dark cathode. *Communications Chemistry*, *2*(1), p.57.

[34] Ibrahim, A.A., Khan, I., Iqbal, N. and Qurashi, A., **2017.** Facile synthesis of tungsten oxide–bismuth vanadate nanoflakes as photoanode material for solar water splitting. *International Journal of Hydrogen Energy*, *42*(5), pp.3423-3430.

[35] Vasilopoulou, M., Soultati, A., Georgiadou, D.G., Stergiopoulos, T., Palilis, L.C., Kennou, S., Stathopoulos, N.A., Davazoglou, D. and Argitis, P., **2014.** Hydrogenated under-stoichiometric tungsten oxide anode interlayers for efficient and stable organic photovoltaics. *Journal of Materials Chemistry A*, *2*(6), pp.1738-1749.

[36] Arumugam, M. and Choi, M.Y., **2020.** Effect of operational parameters on the degradation of methylene blue using visible light active $BiVO_4$ photocatalyst. *Bulletin of the Korean Chemical Society*, *41*(3), pp.304-309.

[37] Hou, J., Wang, Z., Jiao, S. and Zhu, H., 2012. Bi_2O_3 quantum-dot decorated nitrogen-doped Bi_3NbO_7 nanosheets: in situ synthesis and enhanced visible-light photocatalytic activity. *CrystEngComm*, *14*(18), pp.5923-5928.

[38] Lasia, A., **2019.** Mechanism and kinetics of the hydrogen evolution reaction. *International Journal of Hydrogen Energy*, *44*(36), pp.19484-19518.

[39] Van Nguyen, T., Tekalgne, M., Nguyen, T.P., Van Le, Q., Ahn, S.H. and Kim, S.Y., **2023.** Electrocatalysts based on MoS_2 and WS_2 for hydrogen evolution reaction: An overview. *Battery Energy*, *2*(3), p.20220057.

[40] Xiao, P., Buijnsters, J.G., Zhao, Y., Yu, H., Xu, X., Zhu, Y., Tang, D., Zhu, J. and Zhao, Z., **2019.** Fullerene-like WS_2 supported Pd catalyst for hydrogen evolution reaction. *Journal of Catalysis*, *380*, pp.215-223.

[41] Wu, Z., Fang, B., Bonakdarpour, A., Sun, A., Wilkinson, D.P. and Wang, D., **2012**. WS_2 nanosheets as a highly efficient electrocatalyst for hydrogen evolution reaction. *Applied Catalysis B: Environmental*, *125*, pp.59-66.

[42] Su, D., Zhang, X., Wu, A., Yan, H., Liu, Z., Wang, L., Tian, C. and Fu, H., **2019.** CoO-Mo_2N hollow heterostructure for high-efficiency electrocatalytic hydrogen evolution reaction. *NPG Asia Materials*, *11*(1), p.78.

[43] Salvi, P., Nelli, P., Villa, M., Kiros, Y., Zangari, G., Bruni, G., Marini, A. and Milanese, C., **2011.** Hydrogen

evolution reaction in PTFE bonded Raney-Ni electrodes. *International Journal of Hydrogen Energy*, *36*(13), pp.7816-7821.

[44] Hasani, A., Nguyen, T.P., Tekalgne, M., Van Le, Q., Choi, K.S., Lee, T.H., Park, T.J., Jang, H.W. and Kim, S.Y., **2018.** The role of metal dopants in WS_2 nanoflowers in enhancing the hydrogen evolution reaction. *Applied Catalysis A: General*, *567*, pp.73-79.

[45] Mondal, A. and Vomiero, A., **2022.** 2D transition metal dichalcogenides-based electrocatalysts for hydrogen evolution reaction. *Advanced Functional Materials*, *32*(52), p.2208994.

[46] Łosiewicz, B., Budniok, A., Rówiński, E., Łągiewka, E. and Lasia, A., **2004.** The structure, morphology and electrochemical impedance study of the hydrogen evolution reaction on the modified nickel electrodes. *International Journal of Hydrogen Energy*, *29*(2), pp.145-157.

[47] Sarkar, A., Mandal, M.K., Das, S., Mandal, S., Chakraborty, P., Mandal, A., Banerjee, D., Ganguly, S. and Kargupta, K., **2024.** Facile in-situ synthesis of solid mediator based CdS-rGO-WO_3 Z-scheme photocatalytic system for efficient photocatalytic hydrogen generation. *Optical Materials*, *147*, p.114670.